Physics in Medicine & Biology

Improving single-event proton CT by removing nuclear interaction events within the energy/range detector

To cite this article before publication: Lennart Volz *et al* 2019 *Phys. Med. Biol.* in press https://doi.org/10.1088/1361-6560/ab2671

Technical Note: Improving single-event proton CT by removing nuclear interaction events within the energy/range detector

Lennart Volz[1,2], Pierluigi Piersimoni[3], Robert P. Johnson[4], Vladimir A. Bashkirov[5], Reinhard W. Schulte[5] and Joao Seco[1,2]

[1] Department of Biomedical Physics in Radiation Oncology, Deutsches Krebsfoschungszentrum (DKFZ), Heidelberg, Baden-Württemberg, GER
[2] Department of Physics and Astronomy, Heidelberg University, Heidelberg, Baden-Württemberg, GER
[3] Department of Physics and Technology, University of Bergen, Bergen, NO
[4] Santa Cruz Institute for Particle Physics (SCIPP), University of California at Santa Cruz, Santa Cruz, California, USA
[5] Department of Basic Sciences, Division of Biomedical Engineering Sciences, Loma Linda University, Loma Linda, California, USA

E-mail: `l.volz@dkfz-heidelberg.de`

Abstract. Data filtering is crucial for accurate relative stopping power (RSP) reconstruction in proton CT (pCT). In this work, we assess different filters and their performance for the US pCT collaboration prototype pCT system in Monte Carlo (MC) simulations. The potential of using the recently proposed ΔE-E filter for removing nuclear interactions that occurred in the energy/range detector of the pCT system is investigated.

Full pCT scans were acquired with the TOPAS MC simulated version of the prototype scanner that comprises two tracking detectors and a 5 stage energy/range detector. An ideal water cylinder and a water cylinder with 5 tissue inserts were investigated. Before image reconstruction, a $3\,\sigma$ WEPL filter was applied as the only filter, or in addition to filters acting on the energy deposit in each of the energy detector stages, as done currently with the prototype. The potential of the ΔE-E filter that was recently proposed for helium imaging was assessed. The results were compared to simulations for which nuclear interactions were disabled representing ground truth.

The $3\,\sigma$ WEPL filter alone was not sufficient to filter out all nuclear interaction events and systematic fluctuations in the form of ring artifacts were present in the pCT reconstructed images. Applying energy filters currently used with the device prior to the $3\,\sigma$ WEPL filter only slightly improved the image quality. A $2\,\sigma$ WEPL filter improved the mean RSP accuracy, but could not

fully remove the systematic fluctuations. The ΔE-E filter in addition to the current reconstruction procedure efficiently removed the systematic fluctuations and the achieved RSP accuracy closely matched the simulation without nuclear interactions.

This study demonstrates the dependence of the accuracy of the usual $3\,\sigma$ WEPL filter on uncertainties arising within the energy detector. By enabling to remove such uncertainties, the ΔE-E method proved to yield some potential for improving the accuracy of pCT.

Submitted to: *Phys. Med. Biol.*

Keywords: Proton computed tomography, nuclear interactions, relative stopping power, single-event imaging, proton CT detector, Energy telescope

1. Introduction

Proton imaging has gained increasing interest over the last decades. The main advantage of proton CT (pCT) over conventional X-ray CT is the more accurate reconstruction of the voxelized relative stopping power (RSP) information (Hansen et al. 2015) that is crucial for accurate ion beam radiotherapy treatment planning (Paganetti 2012).

While pCT exhibits other benefits (Schulte et al. 2005, Depauw & Seco 2011, Oancea et al. 2018), the achievable spatial resolution is limited due to multiple Coulomb scattering (MCS). To reduce the uncertainty introduced by MCS, in single-event pCT, the trajectory of each proton through the object is estimated during image reconstruction (Williams 2004, Li et al. 2006, Schulte et al. 2008, Erdelyi 2009, Collins-Fekete et al. 2015, Collins-Fekete et al. 2017, Krah et al. 2018). The use of path reconstruction techniques requires sophisticated detector systems capable of acquiring the proton track information before and after the object to be imaged, as well as the residual energy/range on a single-event basis (Schulte et al. 2004, Schulte et al. 2008, Sadrozinski et al. 2013). Additionally, a high precision requirement is placed on the energy/range detector of such a system to ensure accurate RSP reconstruction (Bashkirov et al. 2016b).

However, energy straggling as well as nuclear interactions inside the object to be imaged result in events with an unusually large energy loss and the production of secondary protons that consequently increase the image noise and compromise the RSP accuracy if included in the image reconstruction procedure (Schulte et al. 2005) - see also (Rädler et al. 2018) for a comprehensive analysis of image

noise in proton imaging. In order to ensure high quality pCT images, data filters have to be implemented that accurately identify and remove such events from the recorded particle histories. In most contemporary studies, therefore a $3\,\sigma$ filter on the water equivalent path length (WEPL) crossed by each proton is applied as was proposed by Schulte et al. (2005). Additionally, since the path reconstruction algorithms are based on a Gaussian approximation to MCS, a $3\,\sigma$ filter on the angular displacement of the particles is used to exclude single large angle scattering events (Schulte et al. 2008).

The $3\,\sigma$ WEPL filtering was suggested based on the straggling theory given by Tschalär (1968) and assuming an ideal energy detector (Schulte et al. 2005). However, for energy detectors that require the particles to stop within the detector, nuclear interactions and particles that scatter outside the detector sensitive area increase the weight of the straggling distribution tail compared to the purely electromagnetic expectation. This can largely affect the calculation of the distribution standard deviation, as already pointed out by Tschalär & Maccabee (1970). Hence, while representing relatively few events, nuclear interactions and scattering inside the energy detector could compromise the accuracy of the $3\,\sigma$ WEPL filter and, consequently, the achievable RSP accuracy of the reconstructed image.

The goal of this work was to investigate the effect of such events on the accuracy of pCT with the prototype detector developed by the US pCT collaboration (Bashkirov et al. 2016a, Johnson et al. 2016, Johnson et al. 2017) in Monte Carlo simulations. We investigate the performance of the usual $3\,\sigma$ WEPL filter and assess the potential of using the ΔE-E filtering technique recently proposed to identify nuclear fragmentation events in helium ion CT (HeCT) with the scanner energy/range detector (Volz et al. 2018) to identify nuclear interaction events in pCT.

2. Materials and Methods

2.1. TOPAS simulation setup

The TOPAS simulation toolkit (Perl et al. 2012) release 2.0 patch 3 with Geant4 (Agostinelli et al. 2003, Allison et al. 2006, Allison et al. 2016) version 10.01 patch 02 was used for the Monte Carlo simulations presented in this work. The default "Modular Physics List" of the TOPAS application was activated that has been verified experimentally (Testa et al. 2013). It includes

the following physics lists: G4HadronPhysicsQGSP_BIC_HP, G4DecayPhysics, G4StoppingPhysics for nuclear capture at rest, G4IonBinaryCascadePhysics and G4HadronElasticPhysicsHP for modelling nuclear interactions, as well as G4EmStandardPhysics_option4 for electromagnetic interactions.

The TOPAS simulated version of the US pCT prototype scanner presented in Piersimoni et al. (2017) was used to acquire full pCT scans of two phantoms. The scanner consisted of four position sensitive detector planes, two preceding (front tracker) and two following (rear tracker) the object to be imaged, and a 5-stage energy/range detector. Each of the position sensitive tracker planes comprised two silicon layers ($349 \times 86 \times 0.4\,\mathrm{mm}^3$) used to measure the particle position in vertical and horizontal direction, respectively. Each stage of the energy/range detector consisted of $375 \times 100 \times 50.8\,\mathrm{mm}^3$ blocks of UPS-923A polystyrene scintillator material (simulated using the polystyrene material composition given by the NIST database (Berger et al. 2005)), as well as 65 µm of G4_PMMA wrapping material around each stage (Piersimoni et al. 2017). More details of the pCT prototype scanner design and operation have already been published elsewhere (Bashkirov et al. 2016b, Bashkirov et al. 2016a, Sadrozinski et al. 2016, Johnson et al. 2016, Giacometti et al. 2017, Piersimoni et al. 2017, Johnson et al. 2017).

To investigate the accuracy of the data filters in eliminating nuclear interaction events, we compared the image accuracy to simulations where only electromagnetic interactions were enabled (i.e. activating only G4EmStandardPhysics_option4 in the physics list).

Primaries were generated with an initial energy of 200 MeV and delivered through an ideal flat-field beam configuration (200 mm width, 100 mm height). Full tomographic scans were acquired in 90 individual projections at a 4° angular step as established by Plautz et al. (2016). For each projection, 2×10^6 primary protons were simulated.

To closely model the experimental operation principle, for the different setups the energy output was calibrated to WEPL using a dedicated polystyrene phantom setup. The calibration procedure was originally developed by Bashkirov et al. (2016a); in the present work, the "wedge" calibration procedure described in detail for configuration C in Piersimoni et al. (2017) was followed. The calibration was performed in 5 individual runs: for the first run, two polystyrene wedges (RSP=1.043) providing a continuous thickness variation between 0 and 50.8 mm were placed between the front and rear tracker. In the subsequent runs, 50.8 mm thick blocks of the same polystyrene were added one after another enabling the calibration of the detector over the full range of the particles. During the

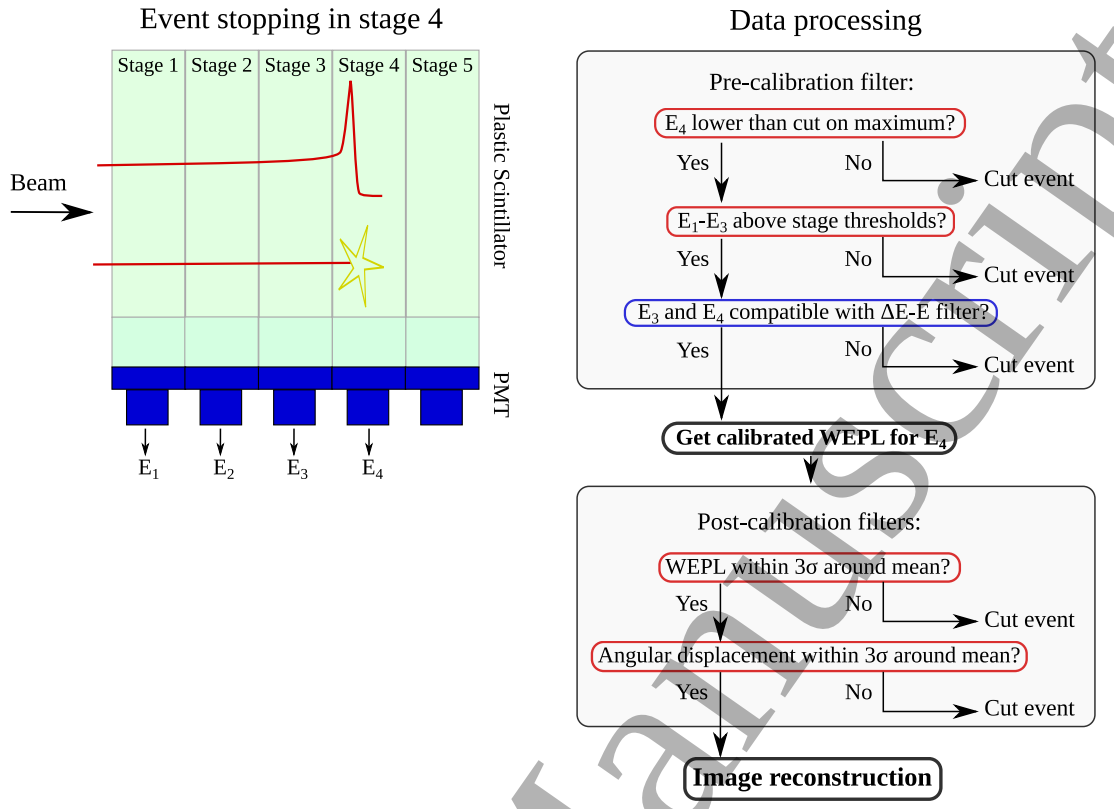

Figure 1. Schematic depiction of the energy/range detector and flowchart of the filtering processes used in this work. The processes outlined in red are used in the current reconstruction procedure for the device. In this work, additionally the recently proposed ΔE-E filter (highlighted in blue) was used to identify such events that suffered a nuclear interaction inside the detector or scattered outside the detector sensitive area (as indicated by the yellow star).

calibration procedure, the particles were binned in a 2D array according to their WEPL and energy deposit to the farthest detector stage in downstream direction they reached into. For each energy bin, the most likely WEPL was computed as the mean within the FWHM bounds of the corresponding WEPL distribution. This resulted in a 340 element vector for each stage that connected the energy deposit in steps of 0.25 MeV from 0 to 85 MeV to the respective most likely WEPL crossed by the particle.

2.2. Image reconstruction and data filtering

Several filters are involved in the current data processing procedure for the prototype detector underlying the investigation in this note. They can be divided into filters that act on the energy loss measurement in the multistage detector before the conversion of the energy loss to WEPL through the derived WEPL calibration (in the following referred to as pre-calibration filters) and filters that act on the calibrated output of the detector (post-calibration filters). The different data filtering processes are explained in figure 1, where the filters currently used with the device are highlighted in red.

Pre-calibration filters For the prototype, first the stage where the particle stopped (henceforth denoted Bragg-peak stage) was determined as the last stage in beam direction in that an energy deposit above 1 MeV was measured. As is implemented in the current pre-processing procedure for the investigated prototype, events with a higher energy deposit in the Bragg-peak stage than transferable by a single proton were removed. Additionally, in the current procedure, an energy threshold filter is implemented, that acts on the energy deposit in each stage leading up to the Bragg-peak stage. For a run without phantom (i.e. a run for that most particles reach into the last detector stage), the mean and standard deviation of the energy deposit in each stage was computed, and the mean minus $5\,\sigma$ was set as the stage threshold. Events with a lower energy deposit in any stage leading up to the Bragg-peak stage compared to the respective stage threshold were removed by the filter.

The data filters mentioned above (threshold energy filter and maximum energy cut) will be referred to as "current" pre-calibration filters throughout this work. However, this refers only to the investigated prototype and does not reflect the reconstruction procedure for other imaging devices.

In order to improve upon the current setup, the recently proposed ΔE-E filtering mode of the detector (Volz et al. 2018) was investigated for its use in proton imaging. For the method, the energy deposit in the Bragg-peak stage was defined as residual energy E and the energy deposit in the stage adjacent in upstream direction as ΔE. Particles that scattered outside the detector sensitive area or those that stopped due to a nuclear interaction could then be identified by comparing the measured ΔE-E relationship with the one expected for protons that stopped in a stage "correctly": In the detector calibration procedure, the ΔE-E response pattern of protons that did not undergo nuclear interactions was

parametrized by a second order polynomial. Events for that the ΔE-E relationship was not compatible with the parametrization within certain margins could then be removed before image reconstruction (compare figure 2).

Image reconstruction and post-calibration filters For each event not removed by the pre-calibration filters, the energy deposit in the Bragg-peak stage was then converted to WEPL using the energy vs. WEPL calibration curves derived in the detector calibration (Piersimoni et al. 2017).

Images were reconstructed using the DROP algebraic reconstruction technique with superiorization of the total variation norm (TVS) (Penfold et al. 2010). The algorithm was run with 40 blocks and stopped after 8 iterations. Proton paths were estimated using the optimized cubic spline path formalism by Collins-Fekete et al. (2015) that was recently shown to be equivalent to the probabilistic most likely path formalism (Collins-Fekete et al. 2017). All images were reconstructed with a slice thickness of 2.5 mm and 256×256 pixel per slice (0.7 mm pixel size). The Feldkamp-David-Kress (FDK) algorithm was used to generate the starting image for the iterative reconstruction. This initial estimate was also used to project the start and end-point of the cubic spline path onto the object hull as described in Schultze et al. (2014).

Within the DROP-TVS algorithm the $3\,\sigma$ WEPL filtering was performed. First, the particle histories were binned based on projection angle (4° bins) and midpoint of the straight line connection between their entrance and exit positions of the reconstruction volume into equal intervals in lateral (1 mm bins) and vertical (2.5 mm bins) coordinates. For each bin, the mode WEPL was identified as the maximum of the WEPL distribution (the maximum with smallest WEPL value should more than one WEPL value contain the maximum number of events). Then, the mean and standard deviation of the WEPL distribution for the bin were computed within $\pm 30\,\%$ around the mode WEPL value. For image reconstruction, only events with a WEPL within $\pm 3\,\sigma$ of their bin mean WEPL were considered. Additionally, in each bin, a $3\,\sigma$ filter on the angular deflection of the particles was applied. In the case where nuclear interactions were disabled in the simulation, only the post-calibration filters were applied.

Investigation of filter efficiency Additionally to comparing the results to a simulation without nuclear interactions, we counted the events that underwent a inelastic/non-elastic nuclear interaction before and after the filtering. This was achieved using the "filtering scorer" framework provided by the TOPAS

Material name	Element(Weight[%])	RSP
Brain tissue	H(8.17);C(53.62);N(1.53);O(26.51);Mg(9.98);Cl(0.19)	1.049
Trabecular bone	H(8.4);C(59.66);N(1.56);O(21.43);Mg(1.46);P(2.33);Cl(0.12);Ca(5.04)	1.112
Cortical bone	H(4.13);C(29.70);N(0.85);O(34.12);Mg(3.11);P(7.57);Cl(0.04);Ca(20.48)	1.591
Tooth enamel	H(2.77);C(21.81);N(0.82);O(34.02);P(12.33);S(0.31);Cl(0.03);Ca(26.60);Ba(1.31)	1.794
Tooth dentin	H(4.51);C(35.36);N(1.23);O(29.41);P(9.20);S(0.08);Cl(0.04);Ca(19.84);Ba(0.33)	1.518

Table 1. Material composition for the insert phantom as used in the simulation. The RSP was calculated directly from the stopping power tables used in the simulation with G4_WATER as reference. The elemental composition was implemented as given in Piersimoni et al. (2017).

toolkit: a filtering scorer was added to the energy/range detector that recorded the energy deposit to the energy/range detector only for particles that originated from inelastic/non-elastic nuclear interactions processes. In processing of the data, a boolean was assigned to each event that was set true, if any energy deposit in any stage was measured for the event with the implemented filtering scorer.

2.3. Simulated Phantoms

First, an ideal water cylinder was investigated, so that the effect of filter uncertainties could be disentangled from the phantom geometry. The cylinder was 150 mm in diameter, 80 mm high and composed of G4_WATER.

To investigate the stopping power accuracy, the insert phantom IP1 presented in Piersimoni et al. (2017) was used. The phantom was a water cylinder (G4_WATER) of 150 mm diameter and 80 mm height with five different tissue inserts of 15 mm radius and 80 mm height: tooth dentin, tooth enamel, cortical bone, trabecular bone and brain tissue, see table 1 for the material composition and reference RSP. To yield an estimate of the RSP accuracy, the mean RSP value was computed in a region-of-interest of 10 mm radius in the center of each insert averaged over the 5 most central slices, and compared to the reference values.

3. Results

3.1. ΔE-E spectra

Figure 2 shows two ΔE-E spectra acquired using a pCT projection of the ideal water cylinder. In figure 2(a), the energy deposition (E_{dep}) to stage 3 was plotted against the energy deposited to stage 2 for all particles stopping in stage 3. For

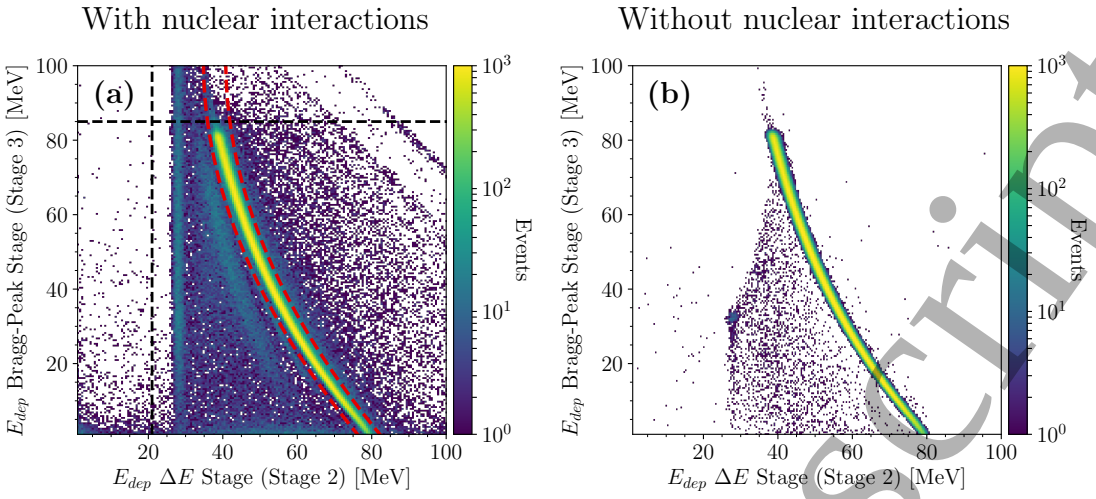

Figure 2. The ΔE-E spectrum for one projection of the ideal water cylinder. **(a)** The energy deposit to stage 3 of all particles stopping in that stage was plotted against their respective energy deposit to stage 2. **(b)** The equivalent for a simulation for that nuclear interactions were disabled. No data filtering was used in acquiring the spectra. The vertical dashed black lines indicate the threshold filter, the horizontal dashed black lines the cut on the maximum transferable energy as used in the current reconstruction procedure with the investigated prototype. The red dashed lines indicate the margins used for the ΔE-E filter.

comparison, in figure 2(b), the equivalent was plotted for a simulation without nuclear interactions.

The dashed black lines in figure 2 indicate the currently used pre-calibration filters (energy threshold and cut on maximum energy). The dashed red lines depict the margins used for the ΔE-E filter. The protons that stopped in stage 3 "correctly", i.e. did not suffer nuclear interactions or scattered outside the detector sensitive area, are seen as the high occurrence pattern. The vertical pattern at $\Delta E \sim 30\,\mathrm{MeV}$ in figure 2(a) corresponded to particles which had crossed a small amount of material or no material at all, and, hence, should have stopped in the last detector stage, but stopped already in stage 3 due to nuclear interactions or scattering. In figure 2(b), the residual noise around the proton occurrence pattern could be removed by excluding particles close to the vertical boundaries of the detector. Therefore, the conclusion was drawn that the residual noise was attributed to events scattering outside the detector sensitive area.

3.2. WEPL calibration curves

In deriving the WEPL calibration curves for each of the 5 stages of the energy/range detector, the effect of the ΔE-E filter was negligible. In the following, therefore, the calibration curves derived with the current calibration procedure of the detector was used for preprocessing all simulations where the full physics list was active. For the simulation where only G4EmStandardPhysics_option4 was active, a separate set of calibration curves was derived and used for the WEPL conversion. Due to the missing elastic nuclear interactions (*hadElastic* physics processes) both in the calibration phantom and inside the detector and the attributed on average slightly lower energy loss of the particles, the calibration curve for the simulation without nuclear interactions was shifted to slightly larger WEPL values at the same energy deposit in the Bragg-peak stage (mean difference $\leqslant$0.22 mm).

3.3. Data filter performance

The effect of the different pre-calibration filters is demonstrated in figure 3. The figure shows the distribution of the converted WEPL crossed by protons that entered the ideal water cylinder in a central region of 5 mm width and 60 mm height (depicted by the drawing on the right side of the figure), i.e. particles that crossed a water equivalent thickness of $\sim$ 150 mm. We note that the so obtained distribution does not correspond directly to the WEPL distributions used for the $3\,\sigma$ WEPL filtering in the DROP-TVS algorithm, where the particles are binned using a finer binning grid as explained above. Different pre-calibration filters were applied before the WEPL conversion: no pre-calibration filtering (blue triangles), the pre-calibration filters currently used with the prototype (green squares) and the ΔE-E filter in addition to the previous (red, circles). For comparison, the figure also shows the equivalent WEPL distribution acquired in a simulation where only electromagnetic interactions were active. At a WEPL of $\sim$ 145 mm, there was a stage interface and consequently, events below or above this value correspond to events that stopped in different stages (stage 2 and 3). This caused the fluctuations observed at the peak of the distribution in Figure 3.

The bottom part of the figure shows the $3\,\sigma$ region around the mean where the different filter setups correspond to the same colors as above. The mean and standard deviations for each distribution are listed in table 2. The WEPL distribution tail was larger for the cases without pre-calibration and the pre-calibration filters currently used with the prototype, when compared to the

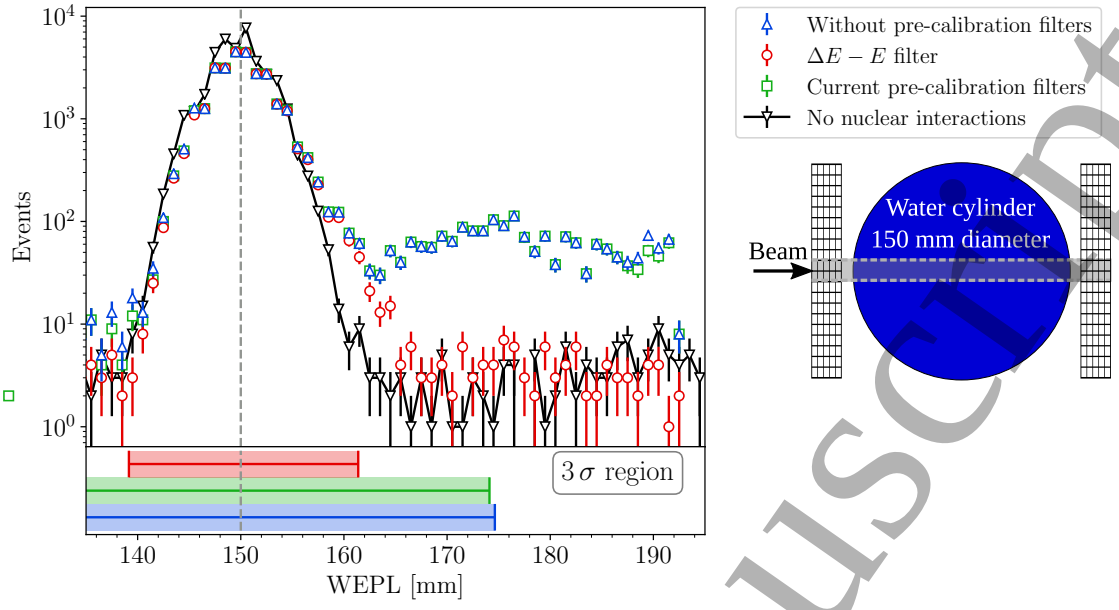

Figure 3. Distribution of WEPL crossed by particles that entered the water phantom in a central region of 5 mm width and 60 mm height indicated by the gray-shaded area in the drawing on the right (not to scale). The blue triangles, the green squares and the red circles mark respectively, the WEPL distribution without pre-calibration filters, the distribution where the current pre-calibration filters were applied, and the distribution after the ΔE-E filter was added to the current pre-calibration filters. The black triangles are the WEPL distribution obtained for a simulation without nuclear interactions. The bottom part of the graph indicates the $3\,\sigma$ regions for the ΔE-E filter (red), for the current pre-calibration filters (green), and the distribution without pre-calibration filters (blue). The errors indicate the standard deviation of the counts. The dashed grey line in the plot depicts the diameter of the water phantom, i.e. the approximate water equivalent thickness crossed by the selected protons.

distribution without nuclear interactions. The ΔE-E filter effectively reduced the tail, which is reflected in the $3\,\sigma$ region: without the ΔE-E filter, the $3\,\sigma$ region still includes events with an unusually large WEPL.

To visualize the nuclear interaction contamination in the final set of events used for image reconstruction, figure 4 shows the resulting ΔE-E spectra for the setup in figure 2(a) after the post-calibration filters were applied in addition to the different pre-calibration filters. In particular, figure 4(a) shows the spectrum after the currently used pre- and post-calibration filters were applied – the threshold filter on the particle energy deposit in the detector stages and the cut on maximum

WEPL distribution	Mean [mm]	Std. dev. [mm]
No pre-calibration filters	151.8	7.6
Current pre-calibration filters	151.9	7.5
Add. ΔE-E filter	150.3	3.5
No nuclear interactions	149.9	3.1

Table 2. Mean and standard deviation for the WEPL distributions indicated in figure 3.

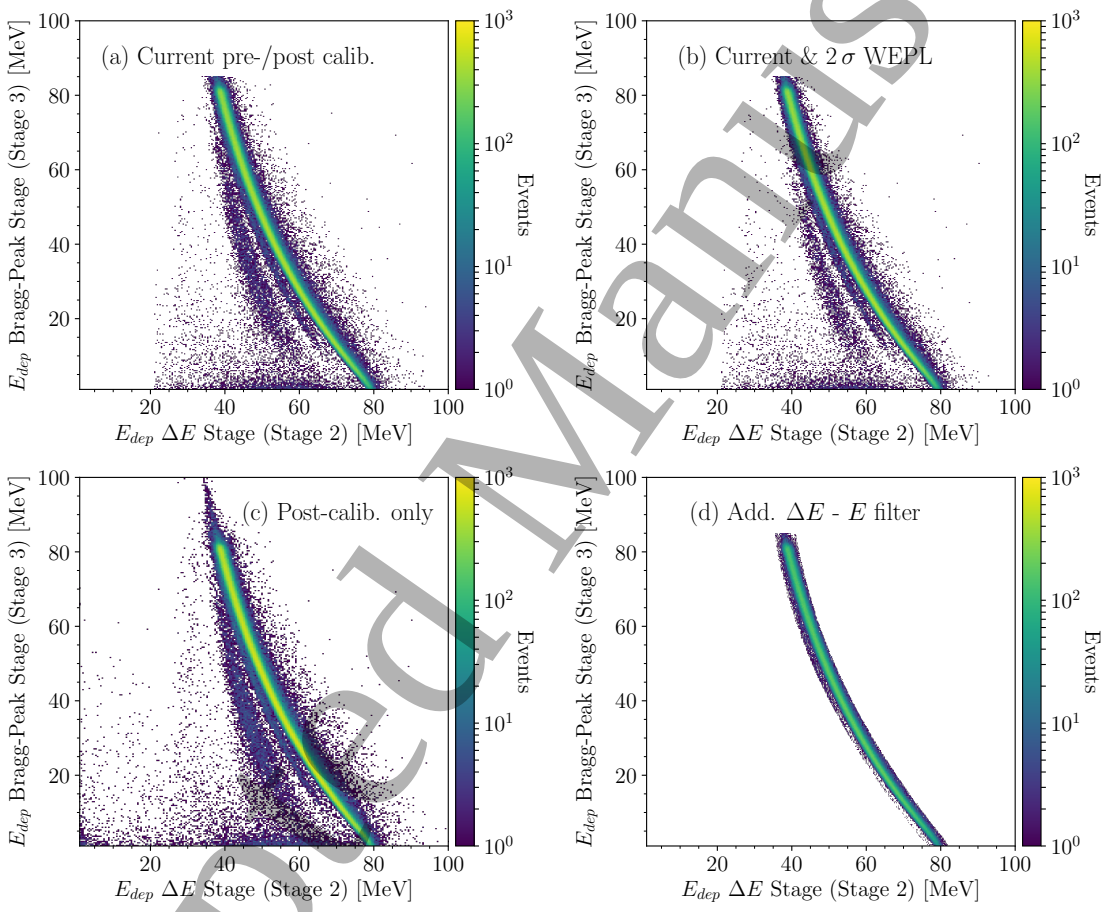

Figure 4. ΔE-E spectrum as shown in figure 2(a) after different data filtering procedures were applied. **(a)** ΔE-E spectrum after the current pre- and post-calibration filtering. **(b)** After the current pre-calibration filters, but using a 2σ WEPL filter in the post-calibration filters. **(c)** Only using the post-calibration filters. **(d)** ΔE-E filter added to the current pre-calibration filters.

transferable energy, as well as the $3\,\sigma$ filters on both angular displacement and WEPL. The currently used filters were not able to remove all nuclear interaction events. For figure 4(b), the same pre-calibration filters as in (a) were applied, but in the post-calibration filters, the $3\,\sigma$ WEPL filter was replaced by a $2\,\sigma$ WEPL filter. While an improvement compared to the current procedure filters was observed, still some nuclear interaction events were left for image reconstruction. In figure 4(c), the post-calibration filters were applied without pre-calibration filters. An increase in nuclear interaction events left for image reconstruction was seen especially at lower ΔE values and also at higher E values, which were previously removed by the threshold filter and maximum cut. Finally, in figure 4(d) the ΔE-E filter was added to the pre-calibration filters. Most nuclear interactions were removed with this setup.

To further quantify the efficiency of the filters, we counted the events that underwent inelastic/non-elastic nuclear interactions for one projection of the ideal water phantom after different filters were applied. The results are listed in table 3. A true positive was defined as an event that remained after filtering and that did not undergo an inelastic/non-elastic nuclear interaction (see section 2.2); a false positive an event that remained but underwent a inelastic/non-elastic nuclear interaction. True/false negatives are equivalently defined for particles that were removed by the filtering.

	Filter	True pos.	False pos.	True neg.	False neg.
Pre-calib.	Current filters	83 %	14 %	3 %	< 1 %
	Add. ΔE-E	80 %	4 %	13 %	3 %
Pre- and post-calib.	Current filters ($3\,\sigma$ WEPL)	72 %	3 %	13 %	12 %
	Current filters ($2\,\sigma$ WEPL)	71 %	2 %	14 %	13 %
	ΔE-E ($3\,\sigma$ WEPL)	71 %	1 %	15 %	13 %

Table 3. Number of events that underwent a inelastic/non-elastic nuclear interaction and were removed/not removed by the current setup of pre- and post-calibration filters, as well as the ΔE-E filter added to the current pre-calibration filters. The values were acquired for one projection of the ideal water cylinder and are relative to the total number of particles that entered the reconstruction field-of-view in that projection.

While the effect of the ΔE-E filter is small relative to the overall number of particles that entered the reconstruction volume, it is important to note, that the filtered events were not evenly distributed in terms of their WEPL. Rather, the number of particles removed by the ΔE-E filter with respect to those used

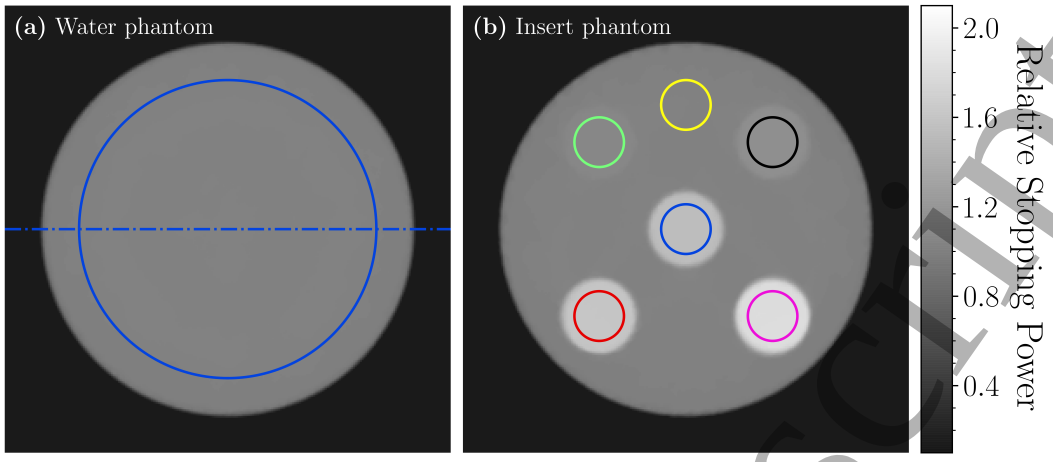

Figure 5. Central slice through the current procedure reconstructed pCT of **(a)** the ideal water phantom and **(b)** the water cylinder with plastic inserts (insert phantom). The blue circle and the dashed blue line in **(a)** show the region-of-interest and line-of-interest used for the acquisition of figure 6, respectively. The circles in **(b)** depict the region-of-interest used for assessing the RSP accuracy (blue: tooth dentine, magenta: tooth enamel, green: brain tissue, red: cortical bone, black: trabecular bone, yellow: water).

for image reconstruction after the current pre- and post-calibration filters were applied peaked at WEPL values that correspond to stage interfaces.

3.4. Accuracy of the reconstructed pCT images

As example reconstructions, figure 5(a) shows the central slice of the pCT current procedure reconstructed image of the ideal water cylinder and figure 5(b) that of the water phantom with different tissue inserts. The effect of different data filters is presented in more detail in the following.

3.4.1. Ideal water phantom Figure 6(a) shows transverse profiles through the pCT images of the water phantom reconstructed with different filtering setups. In the profile of the reconstruction where only the post-calibration filters were used, systematic fluctuations in the form of ring artifacts were present extending to an amplitude of $\sim 0.5\%$ relative to the mean. Using the current pre-calibration filters, these fluctuations were reduced to $\sim 0.3\,\%$ relative to the mean, however, a bias towards overestimated RSP values was present. Note, that these fluctuations

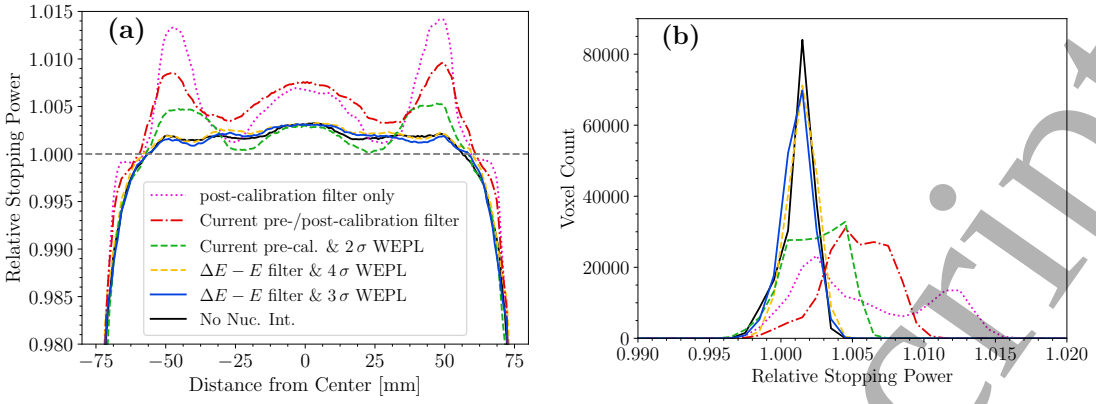

Figure 6. **(a)** Transverse profiles through the pCT reconstructed images of the ideal water cylinder. **(b)** RSP distribution accumulated for every voxel in a central region of interest of 6 cm radius over the 9 most central slices. Different data filtering methods were used to acquire the images: the current pre- and post-calibration filters (dash-dot, red), the current pre-calibration filters with a $2\,\sigma$ WEPL filter (dashed, green), using only post-calibration filters (dotted, magenta), the ΔE-E filter added to the current pre-calibration filters (solid, blue), and the same with a more relaxed $4\,\sigma$ WEPL filter (dashed, yellow). For comparison, the simulation without nuclear interactions is shown (solid, black).

are not visible in figure 5 due to the RSP scale which was chosen to cover all materials of the insert phantom. A $2\,\sigma$ WEPL filter reduced this bias, but did not fully eliminate the systematic fluctuations. The ΔE-E filtering in addition to the currently used filters was able to remove the systematic fluctuations completely. This was the case, even when a more relaxed $4\,\sigma$ WEPL filter was applied.

In figure 6(b) the distribution of reconstructed RSP values in each voxel in a central region of interest of 60 mm radius is shown. The reconstruction in which only the post-calibration filtering was applied yielded a maximum relative error of 1.7 % and the reconstructed RSP values followed no clear trend. Adding the current pre-calibration filters yielded a mean relative error of (0.53 ± 0.23) %, where the given uncertainty is the distribution standard deviation. Using a $2\,\sigma$ WEPL filter in the post-calibration filter setup, the distribution of reconstructed RSP values improved to a mean relative error of (0.24 ± 0.20) %. When the ΔE-E filter was applied in addition to the current pre-calibration filters, the distribution of reconstructed RSP values was much sharper and yielded a mean relative error of (0.11 ± 0.10) %. The ΔE-E method with a more relaxed $4\,\sigma$ WEPL filter yielded similar results with a mean relative error of (0.15 ± 0.10) %. With the ΔE-E filter a similar reconstruction accuracy was achieved as for the simulation without

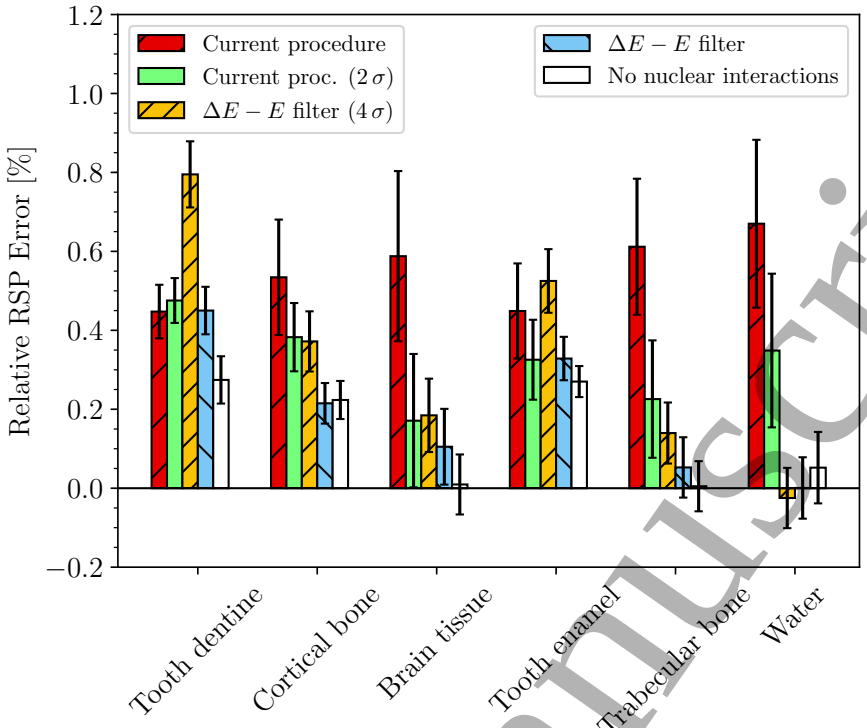

Figure 7. Relative error of the pCT reconstructed RSP values for each tissue insert of the insert phantom for different data filtering modalities. The dashed red bars are the reconstruction with the current pre- and post-calibration filters, the green bars the current reconstruction with a $2\,\sigma$ WEPL filter, the dashed blue bars are the ΔE-E filtered reconstruction and the dashed yellow bars are the ΔE-E filtered reconstruction with a more relaxed $4\,\sigma$ WEPL filter applied. The white bars are the RSP accuracy achieved in a simulation without nuclear interactions. The error bars show the standard deviation.

nuclear interactions.

3.4.2. Insert phantom In figure 7 the relative errors for each of the tissue inserts of the insert phantom are shown for different filtering setups used with the 5 stage energy/range detector. Again, the results are compared against a simulation without nuclear interactions. The mean absolute RSP error resulting from the reconstructions performed using the different filter setups are listed in table 4.

The mean RSP accuracy was lowest for the current procedure data filter setup. A post-calibration filtering with a more strict $2\,\sigma$ WEPL filter in conjunction with the current pre-calibration filters improved the RSP accuracy. The ΔE-E filtering

in addition to the current pre-calibration filters improved the RSP accuracy towards the accuracy achieved in a simulation for that nuclear interactions were disabled. Using a more relaxed $4\,\sigma$ WEPL filter in conjunction with the ΔE-E filtering lowered the RSP accuracy again, especially for the denser material inserts. On the other hand, using the additional ΔE-E filter together with a $2\,\sigma$ WEPL post-calibration filter resulted in the highest mean RSP accuracy. For all data filtering methods, the relative error of the reconstructed RSP was better than the clinically acceptable 1 %.

Filter setup	MAE [%]
Current pre-cal. ($3\,\sigma$ WEPL)	0.55 ± 0.05
Current pre-cal.. ($2\,\sigma$ WEPL)	0.32 ± 0.05
Add. ΔE-E filter ($3\,\sigma$ WEPL)	$\mathbf{0.19 \pm 0.09}$
Add. ΔE-E filter ($4\,\sigma$ WEPL)	0.34 ± 0.14
Add. ΔE-E filter ($2\,\sigma$ WEPL)	0.10 ± 0.06
No nuc. int. ($3\,\sigma$ WEPL)	$\mathbf{0.14 \pm 0.07}$

Table 4. Mean absolute error (MAE) of the reconstructed RSP for the inserts of the insert phantom when different filtering modalities were applied before image reconstruction. The given uncertainty is the standard error of the mean. In parentheses the deviation of the particle WEPL from its mean accepted by the respective post-calibration WEPL filters is indicated.

4. Discussion

In this note, the accuracy of different data filtering setups in removing nuclear interaction events from the primary histories was assessed based on the U.S. pCT collaboration pre-clinical pCT prototype. The benefit the recently developed ΔE-E filter could bring to pCT was investigated.

4.1. Calibration procedure

In acquiring the WEPL calibration curves for the system following the procedure given for configuration C in Piersimoni et al. (2017), applying the ΔE-E filter did not have a significant impact. As explained in section 2, during the calibration procedure of the detector, the particle histories are binned according to their WEPL and energy deposit to the Bragg-peak stage. The calibration for each stage is then found by computing the most likely WEPL for each energy bin.

For protons, the number of events contained in the energy loss distribution tail is much smaller compared to the distribution central part. Hence, WEPL values for that only the energy loss distribution tail overlaps with a given energy bin do not influence the most likely WEPL corresponding to that energy bin, given that all WEPL bins contain a similar number of events. However, the ΔE-E filter by construction acts only on the tail of the energy loss distribution. Therefore, the calibration curves were expected not to be affected much by the ΔE-E filter.

4.2. Image reconstruction

In reconstructing the pCT images, it was seen that the presence of nuclear interactions leads to a larger standard deviation of the WEPL distribution compared to the purely electromagnetic distribution, due to nuclear interaction events increasing the weight of the WEPL distribution tail. Consequently, the post-calibration filters ($3\,\sigma$ WEPL and angular displacement filter) alone were not sufficient in removing events with an unusually large WEPL. This resulted in a reduced RSP accuracy of the pCT reconstructed image. The effect was seen most prominently as systematic fluctuations in the form of ring artifacts arising at stage interfaces, where events stopping in a different stage due to a nuclear interaction can introduce a systematic shift in the WEPL conversion (Bashkirov et al. 2016b). Applying filters on the particle energy deposit measured in the multistage detector as used currently with the investigated prototype only slightly reduced these fluctuations. A $2\,\sigma$ WEPL filter in addition to the current pre-calibration filters improved the image quality, but could not completely remove the systematic fluctuations. Conversely, with the ΔE-E filter applied in addition to the current pre-calibration filters, the tail of the WEPL distribution was reduced towards the distribution where nuclear interactions were disabled in the simulation, thus resulting in a smaller standard deviation and a more effective filtering of events with an unusually large energy loss. With the ΔE-E filter, the systematic fluctuations in the pCT reconstructed images of the ideal water phantom were removed even when a more relaxed $4\,\sigma$ WEPL filter was used. The obtained results closely matched the reconstructed pCT for that nuclear interactions were disabled in the simulation.

Similar results were obtained for the RSP accuracy studied with the insert phantom: the ΔE-E filter added to the current pre-calibration filters improved the RSP accuracy towards the reference value with no nuclear interactions. However, here, a more relaxed $4\,\sigma$ WEPL filter in addition to the ΔE-E filter resulted in

a reduced RSP accuracy, especially for the denser material inserts, where nuclear interactions are more likely to occur. This highlights how the ΔE-E filter cannot replace the $3\,\sigma$ filter, since it cannot remove uncertainties stemming from within the object, but only those arising within the energy/range detector. Not using the $3\,\sigma$ filter in addition to the ΔE-E filtering still results in the issues outlined by Schulte et al. (2005). Using a $2\,\sigma$ WEPL filter together with the ΔE-E filter further improved the accuracy, but also led to the removal of $\sim 7\,\%$ events more compared to the current pre- and post-calibration filter setup. On the other hand, removing the threshold filter from the pre-calibration filters did not degrade the image quality if the ΔE-E filter was used.

For the water phantom, the ΔE-E filter in addition to the pre- and post-calibration filters removed about $4\,\%$ events more with respect to the number of events used in the reconstruction with the current filter setup; a $2\,\sigma$ WEPL filter removed $3\,\%$ events more. The number of particles filtered by the ΔE-E filter with respect to that used with the $2\,\sigma$ WEPL post-calibration filter is not evenly distributed over the full WEPL range, but rather peaks at WEPL values corresponding to stage interfaces of the multistage energy/range detector. On the other hand, for the cylindrical water phantom investigated, the WEPL ranges corresponding to stage interfaces do not correspond to a large fraction of the primary fluence explaining how a low number of events filtered more with the ΔE-E filter can have a noticeable impact on the image quality. We note, that the effect of different filters on the image quality also depends on the reconstruction algorithm used, but the comparison of different reconstruction algorithms was beyond the scope of this work.

4.3. ΔE-E filter

As the the ΔE-E filter was originally proposed for helium imaging with the device, the filtering was performed using only the last two stages the particle reached into which is sufficient to identify helium ions that did not undergo nuclear fragmentation along their path. On the other hand, the more conventional approach to a ΔE-E telescope would be to use the first stage in upstream direction as the ΔE stage and summing up the energy deposits measured in the remaining stages to form E. This, however, could result in a somewhat reduced efficiency of the filter for particles reaching farther into the detector, due to the lower variation of their energy deposit in the first detector stage.

In proton imaging, the main effect of the ΔE-E filter is to remove events

that stopped in a stage due to a nuclear interaction within the energy detector or scattered outside the detector sensitive area. Still, the ΔE-E filter acts only on the last two stages a particle reached into and can hence not remove secondary protons with a range sufficient to traverse more than one detector stage, as these would fall together with the primary proton ΔE-E spectrum. In order to improve upon the current filter setup, additional ΔE-ΔE filters based on the information of the earlier stages could be implemented. However, the results of this work indicate that the potential benefit of this would be minor, as with the current filter setup, already satisfying accuracy was achieved – close to the reference acquired through simulations where nuclear interactions were disabled entirely.

4.4. The impact of nuclear interactions

The key observation in this work is that the calculation of the WEPL standard deviation is sensitive to nuclear interaction events occurring within the energy detector. While the effect on the image quality will be different for other detector designs, the general issue is not limited to the prototype detector investigated here. For energy/range detectors that require the particle to come to a stop within the detector, but provide no longitudinal segmentation (e.g. a one-stage scintillator), filtering out the nuclear interaction contamination stemming from within the energy/range detector would be a more difficult task due to the lack of information. This would also be the case for a classical range telescope, i.e. a stack of thin detector layers providing neither energy nor spatial information, where the range is computed simply from the farthest detector layer the particle reached into. However, the results obtained in this work suggest that for a single stage detector design a $2\,\sigma$ WEPL filter could be a sufficient workaround, as uncertainties remaining after the $2\,\sigma$ WEPL filter were mainly connected to the stage interfaces of the multistage energy/range detector hybrid. Potentially, the optimum would be to implement smart filters, either employing probability measures that correlate the tracker information and the measured WEPL (as e.g. proposed by Collins-Fekete & Romano (2018)) or using machine learning algorithms.

For segmented energy/range hybrid detectors, the ΔE-E filter developed for helium ion imaging was shown to improve also pCT. By removing uncertainties arising from the detector segmentation, the ΔE-E filter potentially further adds to the benefits of using segmented energy/range hybrid detectors outlined by Bashkirov et al. (2016b). However, while nuclear interactions are one cause of uncertainty, for the full experimental setup, additional effects connected to the

detector readout and calibration would have to be taken into account†. The modeling and evaluation of such effects, however, was beyond the scope of this work and will be subject to further investigations.

5. Conclusion

In this work, it was demonstrated that for the prototype system developed by the US pCT collaboration the $3\,\sigma$ filtering alone is not sufficient in removing unusually large energy losses and nuclear interaction events prior to image reconstruction. This resulted in reduced RSP accuracy and systematic fluctuations in the reconstructed images. In general, nuclear interactions inside the energy/range detector influence the calculation of the standard deviation of the WEPL distribution and can reduce the filter efficiency. In this context, the ΔE-E filtering mode was shown to yield some potential for pCT as well, since it enables the identification and effective filtering of nuclear interaction events that occurred within the detector. For single stage detectors, a more strict $2\,\sigma$ filter could potentially act as a workaround. In future studies, the results of this work should be verified in experiment and investigated also for other detector designs.

Acknowledgments

The authors acknowledge Jannis Dickmann for fruitful exchanges regarding the preprocessing procedure of the detector. The authors would like to thank Guillaume Landry and Georgios Dedes for useful discussions. We also thank Lucas Burigo for helpful insights regarding the TOPAS simulation framework. This work was partially supported by grants from the National Institute of Biomedical Imaging and Engineering and the National Science Foundation (NSF) (R01EB013118), the National Cancer Institute (NCI) (1P20183640-01A1), and the United States - Israel Binational Science Foundation (BSF) (2009012 and 2013003).

References

Agostinelli, S., Allison, J., Amako, K., Apostolakis, J., Araujo, H. et al. (2003). Geant4—a simulation toolkit, *Nuclear Instruments and Methods in Physics Research Section A: Accelerators, Spectrometers, Detectors and Associated Equipment* **506**(3): 250–303.

†Such effects can be observed also in Volz et al. (2018) where systematic fluctuations remained in the HeCT reconstructions, even after the ΔE-E filter was applied.

Allison, J., Amako, K., Apostolakis, J., Araujo, H., Dubois, P. A. et al. (2006). Geant4 developments and applications, *IEEE Transactions on Nuclear Science* **53**(1): 270–278.

Allison, J., Amako, K., Apostolakis, J., Arce, P., Asai, M. et al. (2016). Recent developments in geant4, *Nuclear Instruments and Methods in Physics Research Section A: Accelerators, Spectrometers, Detectors and Associated Equipment* **835**: 186 – 225.
URL: *http://www.sciencedirect.com/science/article/pii/S0168900216306957*

Bashkirov, V. A., Johnson, R. P., Sadrozinski, H. F.-W. & Schulte, R. W. (2016a). Development of proton computed tomography detectors for applications in hadron therapy, *Nuclear Instruments & Methods in Physics Research. Section A, Accelerators, Spectrometers, Detectors and Associated Equipment* **809**: 120–129.

Bashkirov, V. A., Schulte, R. W., Hurley, R. F., Johnson, R. P., Sadrozinski, H. F.-W., Zatserklyaniy, A., Plautz, T. & Giacometti, V. (2016b). Novel scintillation detector design and performance for proton radiography and computed tomography, *Medical Physics* **43**(2): 664–674.
URL: *http://dx.doi.org/10.1118/1.4939255*

Berger, M. J., Coursey, J. S., Zucker, M. A. & Chang, J. (2005). *ESTAR, PSTAR and ASTAR: Computer Programs for Calculating Stopping–Power and Range Tables for Electrons, Protons and Helium Ions*, National Institue of Standards and Technology.
URL: *http://physics.nist.gov/Star*

Collins-Fekete, C.-A., Doolan, P., Dias, M. F., Beaulieu, L. & Seco, J. (2015). Developing a phenomenological model of the proton trajectory within a heterogeneous medium required for proton imaging, *Physics in Medicine and Biology* **60**(13): 5071–5082.

Collins-Fekete, C.-A. & Romano, F. (2018). A most likely generating process filter in particle imaging, Presented at the proton imaging workshop Lyon 2018.
URL: *https://protonimaging.sciencesconf.org/213983*

Collins-Fekete, C.-A., Volz, L., Portillo, S. K. N., Beaulieu, L. & Seco, J. (2017). A theoretical framework to predict the most likely ion path in particle imaging, *Physics in Medicine and Biology* **62**(5): 1777.

Depauw, N. & Seco, J. (2011). Sensitivity study of proton radiography and comparison with kV and MV x-ray imaging using GEANT4 Monte Carlo simulations, *Physics in Medicine and Biology* **56**(8): 2407–2421.

Erdelyi, B. (2009). A comprehensive study of the most likely path formalism for proton-computed tomography, *Physics in Medicine and Biology* **54**(20): 6095–6122.

Giacometti, V., Bashkirov, V. A., Piersimoni, P., Guatelli, S., Plautz, T. E. et al. (2017). Software platform for simulation of a prototype proton ct scanner, *Medical Physics* **44**(3): 1002–1016.
URL: *http://dx.doi.org/10.1002/mp.12107*

Hansen, D. C., Seco, J., Sørensen, T. S., Petersen, J. B. B., Wildberger, J. E., Verhaegen, F. & Landry, G. (2015). A simulation study on proton computed tomography (CT) stopping power accuracy using dual energy CT scans as benchmark, *Acta Oncologica* **54**(9): 1638–1642.
URL: *http://dx.doi.org/10.3109/0284186X.2015.1061212*

Johnson, R. P., Bashkirov, V., Coutrakon, G., Giacometti, V., Karbasi, P., Karonis, N., Ordoñez, C., Pankuch, M., Sadrozinski, H.-W., Schubert, K. & Schulte, R. (2017). Results from a prototype proton-ct head scanner, *Physics Procedia* **90**: 209 – 214. Conference on

the Application of Accelerators in Research and Industry, CAARI 2016, 30 October – 4 November 2016, Ft. Worth, TX, USA.
URL: *http://www.sciencedirect.com/science/article/pii/S1875389217302195*

Johnson, R. P., Bashkirov, V., DeWitt, L., Giacometti, V., Hurley, R. F. et al. (2016). A fast experimental scanner for proton ct: Technical performance and first experience with phantom scans, *IEEE transactions on nuclear science* **63**: 52–60.
URL: *http://www.ncbi.nlm.nih.gov/pmc/articles/PMC4844465/*

Krah, N., Khellaf, F., Létang, J. M., Rit, S. & Rinaldi, I. (2018). A comprehensive theoretical comparison of proton imaging set-ups in terms of spatial resolution, *Physics in Medicine & Biology* **63**(13): 135013.

Li, T., Liang, Z., Singanallur, J. V., Satogata, T. J., Williams, D. C. & Schulte, R. W. (2006). Reconstruction for proton computed tomography by tracing proton trajectories: A Monte Carlo study, *Medical Physics* **33**(3): 699.

Oancea, C., Shipulin, K., Mytsin, G., Gao, M., Pankuch, M., Coutrakon, G., Ordonez, C., Johnson, R., Bashkirov, V. & Schulte, R. (2018). Po-0888: Comparison of x-ray ct and proton based ct planning in the presence of titanium dental implants, *Radiotherapy and Oncology* **127**: S470 – S471. ESTRO 37, April 20-24, 2018, Barcelona, Spain.
URL: *http://www.sciencedirect.com/science/article/pii/S0167814018311988*

Paganetti, H. (2012). Range uncertainties in proton therapy and the role of Monte Carlo simulations, *Physics in Medicine and Biology* **57**(11): R99.
URL: *http://iopscience.iop.org/0031-9155/57/11/R99*

Penfold, S. N., Schulte, R. W., Censor, Y. & Rosenfeld, A. B. (2010). Total variation superiorization schemes in proton computed tomography image reconstruction, *Medical Physics* **37**(11): 5887–5895.

Perl, J., Shin, J., Schumann, J., Faddegon, B. & Paganetti, H. (2012). TOPAS: an innovative proton Monte Carlo platform for research and clinical applications, *Medical Physics* **39**(11): 6818–6837.

Piersimoni, P., Ramos-Méndez, J., Geoghegan, T., Bashkirov, V. A., Schulte, R. W. & Faddegon, B. A. (2017). The effect of beam purity and scanner complexity on proton ct accuracy, *Medical Physics* **44**(1): 284–298.
URL: *http://dx.doi.org/10.1002/mp.12013*

Plautz, T. E., Bashkirov, V., Giacometti, V., Hurley, R. F., Johnson, R. P., Piersimoni, P., Sadrozinski, H. F.-W., Schulte, R. W. & Zatserklyaniy, A. (2016). An evaluation of spatial resolution of a prototype proton ct scanner, *Medical Physics* **43**(12): 6291–6300.
URL: *http://dx.doi.org/10.1118/1.4966028*

Rädler, M., Landry, G., Rit, S., Schulte, R. W., Parodi, K. & Dedes, G. (2018). Two-dimensional noise reconstruction in proton computed tomography using distance-driven filtered back-projection of simulated projections, *Physics in Medicine & Biology* **63**(21): 215009.

Sadrozinski, H. F.-W., Geoghegan, T., Harvey, E., Johnson, R. P., Plautz, T. E. et al. (2016). Operation of the preclinical head scanner for proton ct, *Nucl Instrum Methods Phys Res A* **831**: 394–399. 27818559[pmid].
URL: *http://www.ncbi.nlm.nih.gov/pmc/articles/PMC5094456/*

Sadrozinski, H. F.-W., Johnson, R. P., Macafee, S., Plumb, A., Steinberg, D., Zatserklyaniy, A., Bashkirov, V., Hurley, F. & Schulte, R. (2013). Development of a head scanner for proton ct, *Nuclear Instruments & Methods in Physics Research. Section A, Accelerators,*

Spectrometers, Detectors and Associated Equipment **699**: 205–210.

Schulte, R., Bashkirov, V., Tianfang Li, Zhengrong Liang, Mueller, K. et al. (2004). Conceptual design of a proton computed tomography system for applications in proton radiation therapy, *IEEE Transactions on Nuclear Science* **51**(3): 866–872.

Schulte, R. W., Bashkirov, V., Klock, M. C. L., Li, T., Wroe, A. J., Evseev, I., Williams, D. C. & Satogata, T. (2005). Density resolution of proton computed tomography, *Medical Physics* **32**(4): 1035–1046.

Schulte, R. W., Penfold, S. N., Tafas, J. T. & Schubert, K. E. (2008). A maximum likelihood proton path formalism for application in proton computed tomography, *Medical Physics* **35**(11): 4849–4856.

Schultze, B., Witt, M., Censor, Y., Schulte, R. & Schubert, K. E. (2014). Performance of Hull-Detection Algorithms For Proton Computed Tomography Reconstruction, *arXiv:1402.1720 [physics]* .

Testa, M., Schümann, J., Lu, H.-M., Shin, J., Faddegon, B., Perl, J. & Paganetti, H. (2013). Experimental validation of the topas monte carlo system for passive scattering proton therapy, *Med Phys* **40**(12): 121719.
URL: *http://www.ncbi.nlm.nih.gov/pmc/articles/PMC4109425/*

Tschalär, C. & Maccabee, H. D. (1970). Energy-straggling measurements of heavy charged particles in thick absorbers, *Phys. Rev. B* **1**: 2863–2869.
URL: *https://link.aps.org/doi/10.1103/PhysRevB.1.2863*

Tschalär, C. (1968). Straggling distributions of large energy losses, *Nuclear Instruments and Methods* **61**(2): 141 – 156.
URL: *http://www.sciencedirect.com/science/article/pii/0029554X68905351*

Volz, L., Piersimoni, P., Bashkirov, V. A., Brons, S., Collins-Fekete, C.-A., Johnson, R. P., Schulte, R. W. & Seco, J. (2018). The impact of secondary fragments on the image quality of helium imaging, *Physics ind Medicine & Biology* . In Press.

Williams, D. C. (2004). The most likely path of an energetic charged particle through a uniform medium, *Physics in Medicine and Biology* **49**(13): 2899.